Contents lists available at ScienceDirect

Nuclear Instruments and Methods in Physics Research A

Fabrication and characterization of solid-state thermal neutron detectors based on hexagonal boron nitride epilayers

T.C. Doan, S. Majety, S. Grenadier, J. Li, J.Y. Lin, H.X. Jiang *

Department of Electrical & Computer Engineering, Texas Tech University, Lubbock, TX 79409, United States

ABSTRACT

Solid-state thermal neutron detectors with improved detection efficiencies are highly sought after for many applications. Hexagonal boron nitride (hBN) epilayers have been synthesized by metal organic chemical vapor deposition on sapphire substrates. Important material parameters including the mobility-lifetime ($\mu\tau$) product and the thermal neutron absorption length (λ) have been measured. For hBN epilayers with a room temperature resistivity of 5.3×10^{10} Ω cm, the measured $\mu\tau$ product of electrons is 4.46×10^{-8} cm^2/V and of holes is 7.07×10^{-9} cm^2/V. The measured λ values are 277 μm and 77 μm for natural and ^{10}B enriched hBN epilayers, respectively. Metal–semiconductor–metal detectors incorporating 0.3 μm thick hBN epilayers were fabricated. The reaction product pulse-height spectra were measured under thermal neutron irradiation produced by a ^{252}Cf source moderated by high density polyethylene block. The measured pulse-height spectra revealed distinguishable peaks corresponding to the product energies of ^{10}B and neutron reaction with the 0.84 MeV ^{7}Li peak being the most prominent. The detectors exhibited negligible responses to gamma rays produced by ^{137}Cs decay. Our results indicate that hBN epilayers are highly promising for realizing highly sensitive solid-state thermal neutron detectors with expected advantages resulting from semiconductor technologies, including compact size, light weight, ability to integrate with other functional devices, and low cost.

© 2014 Elsevier B.V. All rights reserved.

1. Introduction

Hexagonal boron nitride (hBN) is a wide bandgap semiconductor with an energy band gap around 6 eV. It has emerged as an important material for deep ultraviolet photonic device applications [1–5] and for the exploration of new physical properties in two dimensional systems that are complementary to graphene [6–8]. Due to the fact that the boron-10 (^{10}B) isotope has a capture cross-section of about 3840 barns for thermal neutrons (with 0.025 eV energy) which is orders of magnitude larger than those of most other isotopes [9,10], hBN is also highly promising for the fabrication of solid-state neutron detectors [11,12]. When a ^{10}B atom captures a neutron, it undergoes the following nuclear reaction:

$$^{10}\text{B} + {}_0^1\text{n} \rightarrow {}^7\text{Li}(1.015\,\text{MeV}) + \alpha(1.777\,\text{MeV})\ 6\% \qquad (1a)$$

$$^{10}\text{B} + {}_0^1\text{n} \rightarrow {}^7\text{Li}^*(0.840\,\text{MeV}) + \alpha(1.470\,\text{MeV}).\ 94\% \qquad (1b)$$

The daughter particles (α particles and ^{7}Li ions) produced by the nuclear reaction have a mean free path (or a range) of $\sim$5 μm for

α particles and $\sim$2 μm for ^{7}Li ions [9] and lose their energies by producing a cloud of electron–hole pairs in hBN semiconductor, which serve as the detection signal for thermal neutrons. In hBN neutron detectors, the neutron capture, charge collection, and electrical signal generation occur in the same hBN layer. This is in contrast to boron coated conversion devices, in which the thermal neutron absorption takes place in the boron conversion layer and the generation of electrons and holes occurs in the semiconductor layer [13–15]. Thus, hBN detectors are potentially capable of providing higher detection efficiencies for thermal neutrons than those of the boron coated semiconductor conversion devices. Furthermore, its large energy band gap inherently renders detectors with very low leakage currents [2,11,12,16]. Compared to the commercialized ^{3}He gas filled neutron detectors which have a thermal neutron cross section $\sim$5330 barns [9], the density of ^{3}He gas is significantly lower than the density of ^{10}B in solid state materials such as in hBN. Thus, the thermal neutron absorption length of ^{3}He is much larger than that of hBN. Therefore, ^{3}He gas detectors are generally large and bulky. Most importantly, there is an urgent issue of ^{3}He gas shortage, which limits its future applications.

Our group is currently exploring wafer scale epitaxial growth of hBN semiconductors by metal organic chemical vapor deposition (MOCVD) technique [2–4]. A continuous irradiation with a thermal

* Corresponding author.
E-mail address: hx.jiang@ttu.edu (H.X. Jiang).

neutron beam generated an appreciable steady current response in hBN detectors, corresponding to an effective conversion efficiency approaching ~80% for the absorbed thermal neutrons [11,12]. However, more research is needed to further improve the material quality, device design, and the detection efficiency. In terms of charge carrier collection, neutron detectors operate on the same basic principle as photodetectors. However, the absorption length of thermal neutrons is much larger than the band edge photons in hBN. Therefore, thermal neutron detectors and photodetectors require different design considerations. The typical absorption length of the band edge photons in semiconductors is in the order of 0.1 μm and is only around 15 nm in hBN [2]; while the thermal neutron absorption length (λ) in hBN synthesized using natural boron sources is around 230 μm [11,17]. This large absorption length requires the device design considerations to favor the following: (1) the thickness of hBN layer to be large in order to capture a sufficient number of the incoming neutrons; and (2) the carrier mobility-lifetime product ($\mu\tau$) to be large to allow the free electrons and holes to sweeping out and to be collected as a signal in a timely manner. The $\mu\tau$ product is thus one of the most important parameters that characterize the electronic quality of a semiconductor detector material. This parameter determines the charge collection efficiency and hence the suitability of a material for detector applications. This parameter is significantly influenced by crystalline quality and the density of impurities/defects introduced during the crystal growth and device fabrication processes. Since the hBN epilayer and device technologies are just in the development stage, it is crucial to characterize and optimize the $\mu\tau$ product in order to improve the material quality and device performance. To our knowledge, this parameter has not been characterized for hBN in either bulk or thin film form.
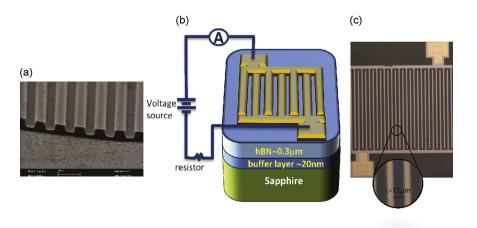
We report here on the growth and characterization of the basic material properties of hBN epilayers that are important for the design of neutron detectors, including the $\mu\tau$ product and thermal neutron absorption coefficient and absorption length of hBN epilayers. Thermal neutron detectors based on a metal–semiconductor–metal (MSM) device architecture have been fabricated. The reaction product pulse height spectra of hBN MSM detectors were tested under thermal neutron irradiation produced by a ^{252}Cf source moderated by high density polyethylene block. The results indicated that neutron detectors fabricated from hBN epilayers are capable of resolving the prominent energy peaks as expected from the reaction of Eq. (1) with high spectral resolution.

2. Epilayer growth and basic structural properties

The hBN epilayers employed in this study were grown by MOCVD on *c*-plane electrically insulating crystalline sapphire substrates. Since hBN materials and devices are in the development stage, the use of the insulating sapphire substrates is more suitable for the thorough characterization of the material properties of hBN for neutron detector applications. Triethylboron (TEB) and ammonia (NH_3) were used as precursors for boron and nitrogen, respectively. Due to the lattice mismatch between hBN and Al_2O_3, a low temperature BN buffer layer of about 10 nm in thickness was deposited on sapphire substrate at 600 °C prior to the growth of hBN epilayer. The hBN epilayers were grown at 1300 °C using hydrogen as a carrier gas. X-ray diffraction (XRD) θ–2θ scan of the grown hBN [4] revealed a *c*-lattice constant ~6.67 Å, which closely matches the bulk *c*-lattice constant of hBN (c=6.66 Å) [18–20], affirming that our MOCVD grown BN films are of single hexagonal phase. The XRD rocking curve (ω-scans) of the (0002) diffraction peak of hBN exhibited a full width at half maximum (FWHM) of 380 arcsec [4], which is comparable to those of typical GaN epilayers grown on sapphire [21], but is much broader than the typical FWHM (~63 arcsec) of high quality AlN grown on sapphire [22]. The results are indicative of the fact that the development of epitaxial layers of hBN is in its early stage. Secondary ion mass spectrometry (SIMS) results revealed that hBN epilayers have excellent stoichiometry [4]. The grown epilayers also have a good surface morphology as indicated by the scanning electron microscopy (SEM) image of an hBN epilayer (etched into stripes) shown in Fig. 1(a).

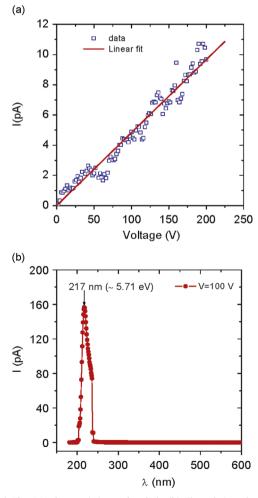## 3. Device fabrication and mobility and lifetime product characterization

Metal–semiconductor–metal (MSM) detectors with interdigital fingers were fabricated from these hBN epilayers with etched stripes (as illustrated in Fig. 1(a)) based on the processes outlined in Ref. [11,16] to take the advantage of the excellent lateral transport properties of hBN. Fig. 1(b) shows the schematics of the hBN layer structure employed for MSM detector fabrication and the setup for the *I–V* characteristics measurements. The devices incorporate hBN epilayers with 0.3 μm in thickness. Since the development of hBN epilayers is in its early stage, the surface morphology of hBN epilayers becomes poorer with an increase in

Fig. 1. (a) SEM image of an hBN epilayer etched into stripes. (b) Schematic diagram of the layer structure of hBN epilayer employed for MSM detector fabrication and the setup for the *I–V* characteristics measurements. (c) Optical microscopy image of a fabricated MSM detector with a device size of 500 × 500 μm² and 6 μm/12 μm finger width/spacing.

hBN layer thickness. Therefore, in selecting the hBN epilayer thickness for detector fabrication, we considered the trade-off between ensuring the highest material quality and a sufficient layer thickness for appreciable thermal neutron absorption. Fig. 1 (c) is a micrograph of a fabricated MSM detector. The detector has a dimension of $500 \times 500\ \mu m^2$. The width of the metallic inter-digital fingers is about $6\ \mu m$ while the spacing between the fingers is about $L=12\ \mu m$. The metallic inter-digital fingers consist of a Ti/Al bilayer (20 nm/30 nm) deposited by e-beam evaporation. Fig. 2(a) shows the dark I–V characteristics of the fabricated detector from which a resistivity of about $5.3 \times 10^{10}\ \Omega\ cm$ was obtained from the geometrical configuration of hBN epilayers. The relative photospectral response of the hBN detector shown in Fig. 2(b) exhibits a peak responsivity at 217 nm and a cut-off wavelength at around 230 nm. There are virtually no detectable responses for below bandgap excitation measured up to 600 nm. The system for the photospectral response measurements consists of a broad spectrum light source covering from 170 to 2100 nm (model EQ-99 Laser-Driven Light Source (LDLS) by Energetiq), monochromator, source-meter, and electrometer. LDLS was dispersed by the monochromator to obtain light with different wavelengths.

In terms of the detector applications, it is crucial to sweep-out the free electrons and holes generated by the nuclear reaction in a timely manner. Most of the electrons and holes will be collected by the electrodes if the carrier transit time (τ_t) through the material is smaller than the recombination (or trapping) time of electrons and holes (τ). The relationship between the carrier transit time and mobility, μ, is described by the following equation:

$$\tau_t = \frac{L}{\mu E} = \frac{L^2}{\mu V}, \tag{2}$$

where V and E are the applied voltage and electric field, respectively, and L is the distance between the two electrodes. Therefore the mobility-lifetime product ($\mu\tau$) determines the average distance traveled by the free carriers per unit electric field before recombination or trapping occurs. Most of the free carriers can be collected by the electrodes if the recombination or trapping time is larger than the transit time $\tau > \tau_t$, or equivalently if

$$\mu\tau \geq \frac{L^2}{V}. \tag{3}$$

To determine if the quality of these MOCVD grown hBN epilayers is sufficiently good for detector fabrication, we re-write Eq. (3) in terms of the relationship between the $\mu\tau$ product and in-plane resistivity (in units of Ω cm) [23] of hBN epilayers which have a dark current of 10 pA for a rectangular slab with a cross section area of $A=0.30 \times 500\ \mu m^2 = 1.5 \times 10^{-6}\ cm^2$, and $L=12\ \mu m$, as

$$\mu\tau \geq \frac{L^2}{V} = \frac{LA}{\rho I} = \frac{12 \times 10^{-4} \times 1.5 \times 10^{-6}}{10 \times 10^{-12}}\frac{1}{\rho} = \frac{180}{\rho}\ (cm^2/V). \tag{4}$$
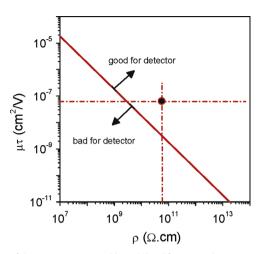
Eq. (4) provides the minimum acceptable mobility-lifetime product. The result of Eq. (4) is plotted in Fig. 3 and is a straight line. The plot means that if the $\mu\tau$ products of our hBN epilayers fall into the area above (below) the line, the materials are satisfying (are not satisfying) the minimum requirements for detector applications.

To measure the $\mu\tau$ products, the same broad spectrum LDLS (EQ-99 by Energetiq) was used to illuminate the whole area of the hBN MSM device. Photo-generated electrons and holes are drifted to the electrodes by the applied electric field. The photocurrent is described by the Many' equation [24,25]
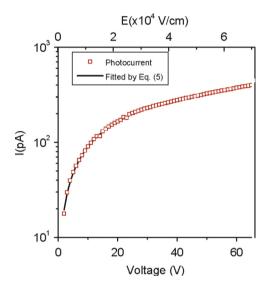
$$I(V) = I_o \left[\frac{\mu_n\tau_n V}{L^2} - \left(\frac{\mu_n\tau_n V}{L^2}\right)^2 e^{-\frac{L^2}{\mu_n\tau_n V}} + \frac{\mu_p\tau_p V}{L^2} - \left(\frac{\mu_p\tau_p V}{L^2}\right)^2 e^{-\frac{L^2}{\mu_p\tau_p V}} \right], \tag{5}$$

where $\mu_n\tau_n$ and $\mu_p\tau_p$ are the mobility-lifetime product of electrons and holes, respectively. I_o is the saturation current.

The first (last) two terms are the contributions of the photo-generated electrons (holes) and $\mu\tau$ products for electrons and holes can thus be obtained by fitting the measured I–V curve with Eq. (5). In Fig. 4, we plot the measured photocurrents under different bias voltages and applied electric fields for a representative hBN MSM device. It shows that the photocurrent increases with an increase of the applied electric field $E\ (=V/L)$ and it approaches to a saturation value at $E \sim 6 \times 10^4$ V/cm. The solid curve is the least squares fit of data (open squares) using Eq. (5). The fitted $\mu\tau$ product of electrons is $\mu_n\tau_n = 4.5 \times 10^{-8}$ cm^2/V and of holes is $\mu_p\tau_p = 7.1 \times 10^{-9}$ cm^2/V. From the $\mu\tau$ products, we can also deduce the diffusion lengths of electrons and holes at room temperature to be 0.34 μm and 0.14 μm, respectively. The $\mu_n\tau_n$ product value for electrons ($\mu_n\tau_n = 4.5 \times 10^{-8}$ cm^2/V) is indicated as a dot in Fig. 3 for our hBN epilayers (with $\rho = 5.3 \times 10^{10}\ \Omega$ cm), which falls into the area above the straight line. The $\mu\tau$ products are expected to further improve as the material quality of our hBN epilayers continues to improve. However, the results obtained from Figs. 3 and 4 indicate that the quality of our current epilayers is sufficiently good for the fabrication of neutron detectors for basic properties characterization as well as for prototype device demonstration.

Fig. 2. (a) The I–V characteristics under dark. (b) The relative photo-spectral response of an hBN MSM detector.
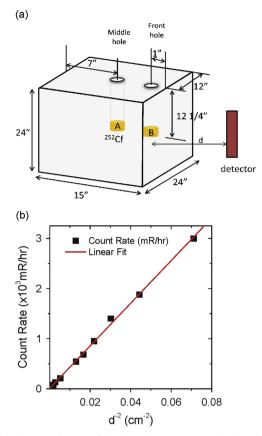
Fig. 3. Plot of the minimum acceptable mobility-lifetime product versus resistivity for the hBN epilayers (with dark current 10 pA, film thickness 0.3 μm, and a cross section area of $0.3 \times 500 \, \mu m^2$ and the distance between the two electrodes $L = 12 \, \mu m$).

Fig. 4. Semi-log plot of I–V characteristics under photoexcitation: squares are the measured photocurrents and the solid curve is the least squares fitting of data with Eq. (5). The size of the squares indicates the size of the error bar of the data points.

4. Pulse-height spectra

To measure the reaction product pulse-height spectra of hBN detectors, a Californium-252 source of 4.4 μg corresponding to 2.4 mCi of radiation activity was used as a neutron source. The source emits $\sim 1.1 \times 10^7$ neutron/second with an average energy at about 2 MeV and a half life of 2.4 years. A high-density-polyethylene (HDPE) moderator was constructed to reduce the neutron energy to that of thermal neutrons [26,27]. The schematic diagram of the neutron source setup is shown in Fig. 5(a). Fig. 5(b) shows the thermal neutron counting rate (mR/h) measured at different distance (d) from the ^{252}Cf source using a standard thermal neutron detector (Model 2241-4 Ludlum Inc.). In conducting the measurements, the ^{252}Cf source was placed inside the moderator and 3 cm away from the front of the moderator's surface. The calibration results indicate that the rate is inversely proportional to d^2. A linear relationship between the thermal neutron count rates versus d^{-2} shows that the ^{252}Cf source within the moderator can be considered as a point source of thermal neutrons for points outside the HDPE box. The flux of the thermal neutrons at a distance d from the ^{252}Cf source can be described by

Fig. 5. (a) Schematic diagram of the thermal neutron source (produced by ^{252}Cf in conjunction with a high-density-polyethylene (HDPE) moderator) utilized in this study. (b) Thermal neutron count rate vs d, the distance between the detector and the moderator surface as indicated in Fig. 5(a).
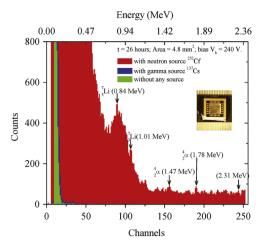
the following equation:

$$\Phi_1 = \Phi_2 \frac{d_2^2}{d_1^2} \tag{6}$$

where Φ_1, Φ_2 are the flux of thermal neutrons at distances d_1 and d_2, respectively. It is expected that every neutron from ^{252}Cf source will convert into 2.35×10^{-4} thermal neutron at a point in the air that is 10 cm away from the moderator's surface [26].

For the pulse-height spectra measurement, a detector with a relatively large device area of 4.8 mm^2 was fabricated and bonded in a ten pin ceramic flat pack for characterization (inset of Fig. 6). Notice that the large area detector has the same dark current density and $\mu\tau$ product as the small area detectors. The detector was placed inside a metal box to reduce the electronic noise and connected to a charge sensitive modified preamplifier (Cremat, Inc.) with time constant of 45 ns and a pulse shaping amplifier with a 6 μs shaping time. The pulse-height spectra were measured with a multi-channel analyzer (MCA) (model 8000D by Amptek). To maximize the signal, the detector was placed close to the front of the moderator's surface (3 cm away from the source). The thermal neutron flux at the detector point is $\Phi_1 = 1.1 \times 10^7 \times 2.35 \times 10^{-4} \times 13^2/3^2 = 4.85 \times 10^4$ (neutron/cm^{2}s). Due to the highly resistive nature of the undoped hBN epilayers, the detector was biased at 240 V and the counts were measured continuously for 26 h ($t = 9.36 \times 10^4$ s). The total number of thermal neutron absorbed by the detector, therefore, can be estimated according to the following equation:

$$n_{abs} = \Phi_1 A (1 - e^{-d/\lambda}) t = 2.36 \times 10^5, \tag{7}$$

where $\Phi_1 = 4.85 \times 10^4$ neutron/cm^{2}s is the thermal neutron flux at the detector position (3 cm from the ^{252}Cf source), $A = 4.8$ mm^2 is the

Fig. 6. Pulse height spectrum of thermal neutrons measured with an hBN MSM neutron detector. Blue – background counts; green – under γ-ray irradiation produced by ^{137}Cs decay; red – under neutron irradiation produced by a [252]Cf source moderated by high density polyethylene block of Fig. 5(a). (For interpretation of the references to color in this figure, the reader is referred to the web version of this article.)

detector area, and $t = 9.36 \times 10^4$ s is the total counting time, $d = 0.3$ μm is the thickness of hBN epilayers, and $λ = 277$ μm is the measured thermal neutron absorption length. The blue and red column bars in Fig. 6 are the total counts measured in the absence and presence of the [252]Cf source, respectively, and the green column bars represent the measured counts while the detector was only irradiated by a γ-ray source (^{137}Cs). In the absence of the [252]Cf source, the counts are just background noise and no counts were observed beyond channel 25. Under the thermal neutron irradiation, we believe that hBN detectors have resolved the four reaction product energies in Eq. (1).

The most dominant peak in Fig. 6 is at channel 89, which based on the system calibration, corresponds to 0.84 MeV (1/106 MeV per channel). This peak is a measure of the kinetic energy of [7]Li ions, resulting from the nuclear reaction (with 94% probability) of Eq. (1b). A weaker peak at channel 156 is associated with 1.47 MeV α particles as expected from the nuclear reaction (with 94% probability) of Eq. (1b). Two additional weaker peaks at channels 107 and 189 can be attributed, to the kinetics energies of 1.01 MeV [7]Li and 1.78 MeV α particles as expected from the nuclear reaction with a lower (6%) probability of Eq. (1a). The sum peak at 2.31 MeV as expected from the nuclear reaction (with 94% probability) of Eq. (1b) is not distinguishable. For the dominant nuclear reaction (with 94% probability) of Eq. (1b), we expect that our detectors are less sensitive to pick up the 1.47 MeV α peak because the mean free path (or the range) of α particles in boron based semiconductors is about 2 times larger than that of [7]Li ions (∼5 μm for α particles vs ∼2 μm for [7]Li ions) [9,28] and the detector thickness is only 0.3 μm. This combination makes the probability for detecting the α particles lower than for the 0.84 MeV [7]Li ions. Similarly, it is difficult for this set of devices to clearly resolve the sum peak at 2.31 MeV. Nevertheless, it is apparent that the hBN detector provides a total counts that is well above the noise level (above channel 25). In order to resolve all reaction product peaks expected from Eq. (1) unambiguously, the detectors must incorporate thicker hBN epilayers or [10]B enriched hBN epilayers.

It is interesting to note that the observed peaks are quite narrow, which can be understood by considering the fact that the nuclear reaction and free carrier generation occur in the same hBN layer. This is in contrast to boron coated or perforated conversion devices [13–15,27,29,30] in which the [7]Li and α particles created at the nuclear reaction site in the conversion layer must travel a certain distance before reach to the semiconductor layer to generate electrons and holes, during which [7]Li and α particles

loss energies and the detected pulse-height spectra generally are broadened due to this energy dispersion process. In this sense, hBN semiconductor detectors are much more sensitive to resolve energies of specific reaction products than conversion devices. On the other hand, in contrast to other boron compounds (e.g., $B_{12}As_2$ and B_4C) [31–34], the simple crystal structure of hBN allows the attainment of single crystalline thin films by MOCVD technique. Materials with single crystalline structure contain few charge traps and allow a more rapid sweep-out of the electrons and holes generated by the nuclear reaction. Furthermore, as seen from Fig. 6, the hBN detector has a negligible response to γ-ray produced by ^{137}Cs decay with an energy at 0.662 MeV. This fact has not been previously demonstrated, but is expected because BN is composed of low atomic number elements, B(5) and N(7), BN's interaction with γ rays should be low. Thus, hBN devices will have an excellent ability to discriminate between γ and neutron radiation. These properties together may be utilized to design spectrally sensitive neutron detectors.

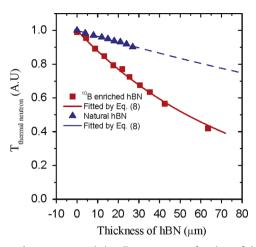## 5. Thermal neutron absorption lengths in natural and [10]B enriched hBN

An effective way to gain neutron detection efficiency is by [10]B isotopic enrichment of the source molecule, which can increase the neutron absorption efficiency with little impact on the semiconducting properties. We have carried out preliminary studies on the MOCVD growth of [10]B isotopic enriched hBN epilayers. As of this writing, we have not yet carried out device fabrication for [10]B enriched hBN epilayers. [10]B enriched trimethylborane (TMB): $B(CH_3)_3$ with a [10]B purity of 99.5% (from Voltaix, LLC) was used as B precursor for the growth of [10]B enriched hBN epilayers. It is expected that the use of a [10]B enriched (100% [10]B) source for B precursor will reduce the epilayer thickness requirement by a factor of 5. This also means that the thermal absorption length of [10]B enriched hBN epilayer is 5 times smaller than the natural hBN. Boron density in hBN is about 5.5×10^{22} cm^{-3} [9] in which isotope [10]B is about 20% and isotope [11]B is about 80%. Therefore, the density of isotope [10]B atoms in hBN is about $N = 1.1 \times 10^{22}$ cm^{-3}. A microscopic neutron absorption coefficient (α) and absorption length (λ) in a natural hBN are thus: $\alpha_{natural} = N\sigma = 42.24$ cm^{-1} and $\lambda_{natural} = 1/\alpha_{natural} = 2.37 \times 10^{-2}$ cm $= 237$ μm, where $\sigma = 3840$ barns $\sim 3.84 \times 10^{-21}$ cm^2 is the cross section of [10]B for thermal neutron (25.3 meV). For [10]B enriched hBN (close to 100% [10]B), neutron absorption coefficient (length) will be a factor of 5 larger (smaller). Thus, we have

$$\alpha_{enriched} = 5\alpha_{natural} = 211.20 \text{ cm}^{-1} \text{ and } \lambda_{enriched} = \frac{1}{\alpha_{enrich}} = 4.73$$
$$\times 10^{-3} \text{ cm} = 47 \text{ } \mu m.$$

the thermal neutron transmission measurements of both natural and [10]B enriched of hBN epilayers were carried out at TRIGA Mark II Reactor at Kansas State University. The thermal neutron (25.3 meV) flux was set to about 6.2×10^4/cm^2 s for the measurements. The layer thickness variation was obtained by stacking together multiple hBN epilayers (grown on sapphire substrates). The data marked by squares and triangles in Fig. 7 are the measured transmission coefficients of [10]B enriched and natural hBN, respectively. It has been checked that sapphire substrates have no effect on thermal neutron absorption. The solid and dash curves are the least squares fitting of data with the following equation:

$$I(d) = I_0 e^{-\frac{d}{\lambda}}, \tag{8}$$

where d is thickness of hBN epilayers, λ is the absorption length. From these data, we obtain the thermal neutron absorption lengths of 77 μm and 277 μm for [10]B enriched and natural hBN epilayers, respectively. Hence, we have experimentally achieved a reduction by

Fig. 7. Thermal neutron transmission, $T_{thermal\ neutron}$, as functions of the epilayer thickness for natural and ^{10}B enriched hBN epilayers. The solid squares and triangles are data and the solid curves are the least squares fitting of data with Eq. (8).

a factor of about 4 in the thermal neutron absorption length in ^{10}B enriched hBN compared to natural hBN. In principle, a factor of 5 reduction in thermal neutron absorption length is expected by ^{10}B isotopic enrichment of the source molecule. The discrepancy may be due to the presence of a small fraction of fast neutrons in addition to the thermal neutrons in the neutron source, material quality, uncertainty in determining hBN layer thickness, and the actual ^{10}B precursor enrichment is less than 100%. However, the feasibility of producing wafer scale ^{10}B enriched hBN epilayers will open up new opportunities for realizing solid-state neutron detectors with improved efficiencies.

6. Summary

In summary, hBN epilayers have been grown on sapphire substrates by MOCVD and explored for solid-state thermal neutron detector applications. Mobility-lifetime ($\mu\tau$) products of electrons and holes of hBN epilayers were characterized and the results indicate that these MOCVD grown hBN epilayers are suitable for detector fabrication. Metal–semiconductor–metal (MSM) detectors were fabricated. As deep UV photodetectors, these devices exhibit a peak responsivity at 217 nm and a cut-off wavelength at around 230 nm with virtually no responses for $\lambda > 230$ nm. The fabricated hBN MSM detectors were employed for thermal neutron detection and the measured pulse-height spectra exhibit distinguishable peaks due to the detection of the four product energies expected from the ^{10}B and neutron reaction. Among the reaction product energies, the 0.84 MeV ^{7}Li ions peak is most prominent. The 1.47 MeV α peak and hence the sum peak at 2.31 MeV are much weaker due to the combination of the larger range of α particles than ^{7}Li ions in hBN and the fabricated detectors incorporating hBN epilayers with only 0.3 μm in thickness. Furthermore, hBN detectors show a negligible response to 0.662 MeV γ-rays produced by ^{137}Cs decay and hence are expected to provide an excellent ability to discriminate between γ and neutron radiation. ^{10}B enriched hBN epilayers have been synthesized. A 4-fold reduction in the thermal neutron absorption length in ^{10}B enriched hBN over natural hBN has been obtained. Since research of semiconducting hBN solid-state neutron detectors is in its very early stage, many issues merit further studies. Further improvements in material quality, conductivity control, and post-growth material and contact processes would enhance the properties of hBN for detector applications. Due to its layered structure, it is also of paramount importance to investigate the vertical

transport properties of hBN and to elucidate the effects of the vertical transport properties on the performance of detectors with large layer thicknesses. With further developments in material growth and device design such as incorporating ^{10}B enriched epilayers with increased layer thickness (or multi-stacked ^{10}B enriched epilayers) and crystalline quality, hBN semiconductor detectors with neutron detection sensitivity greatly exceeding those of the current state-of-the-art are anticipated. The ability of producing wafer scale hBN semiconductor materials by techniques such as MOCVD and the applicability of semiconductor processing technologies also open up the possibility to construct sophisticated neutron detectors with high sensitivity at relatively low costs.

References

[1] K. Watanabe, T. Taniguchi, H. Kanda, Nature Materials 3 (2004) 404.
[2] J. Li, S. Majety, R. Dahal, W.P. Zhao, J.Y. Lin, H.X. Jiang, Applied Physics Letters 101 (2012) 171112.
[3] S. Majety, X.K. Cao, J. Li, R. Dahal, J.Y. Lin, H.X. Jiang, Applied Physics Letters 101 (2012) 051110.
[4] R. Dahal, J. Li, S. Majety, B.N. Pantha, X.K. Cao, J.Y. Lin, H.X. Jiang, Applied Physics Letters 98 (2011) 211110.
[5] K. Watanabe, T. Tanniguchi, Physical Review B 79 (2009) 193104.
[6] N. Alem, R. Erni, C. Kisielowski, M.D. Rossell, W. Gannett, A. Zettl, Physical Review B 80 (2009) 155425.
[7] C.R. Dean, A.F. Young, I. Meric, C. Lee, L. Wang, S. Sorgenfrei, K. Watanabe, T. Taniguchi, P. Kim, K.L. Shepard, J. Hone, Nature Nanotechnology 5 (2010) 722.
[8] A.K. Geim, I.V. Grigorieva, Nature 499 (2013) 419.
[9] G.F. Knoll, Radiation detection and measurement, 4th edition, John Wiley & Sons, 2010.
[10] O. Osberghaus, Zeitschrift fuer Physik 128 (1950) 366.
[11] J. Li, R. Dahal, S. Majety, J.Y. Lin, H.X. Jiang, Nuclear Instruments and Methods in Physics Research A 654 (2011) 417.
[12] S. Majety, J. Li, X.K. Cao, R. Dahal, J.Y. Lin, H.X. Jiang, Proceedings of SPIE, 8507, 85070R.
[13] A. Rose, Nuclear Instruments and Methods 52 (1967) 166.
[14] R.J. Nikolic, Chin Li Cheung, C.E. Reinhardt, T.F. Wang, Proceedings of SPIE, 6013, 601305.
[15] H.K. Gersch, D.S. McGregor, P.A. Simpson, Nuclear Instruments and Methods in Physics Research A 489 (2002) 86.
[16] S. Grenadier, J. Li, J.Y. Lin, H.X. Jiang, J. Vac. Sci. Technol. A 31 (2013) 061517.
[17] J. Uher, S. Pospisil, V. Linhart, M. Schieber, Applied Physics Letters 90 (2007) 124101.
[18] R.S. Pease, Acta Crystallographica 5 (1952) 356.
[19] S.L. Rumyantsev, M.E. Levinshtein, A.D. Jackson, S.N. Mohammmad, G.L. Harris, M.G. Spencer, M.S. Shur, in: M.E. Levinshtein, S.L. Rumyantsev, M.S. Shur (Eds.), Properties of Advanced Semiconductor Materials GaN, AlN, InN, BN, SiC, SiGe, Wiley, New York, 2001, pp. 67–92.
[20] R.W. Lynch, H.G.J. Drickamer, Journal of Chemical Physics 44 (1966) 181.
[21] S. Nakamura, G. Fasol, S.J. Pearton, The Blue Laser Diode: The Complete Story, Springer, New York, 2000.
[22] B.N. Pantha, R. Dahal, M.L. Nakarmi, N. Nepal, J. Li, J.Y. Lin, H.X. Jiang, Q.S. Paduano, David Weyburne, Applied Physics Letters 90 (2007) 241101.
[23] W.C. Mcginnis, R. Clarke, C. Cionca, and R. Brockus, Film Implementation of a neutron detector (FIND): Critical Materials properties Technical Report. 2007.
[24] A. Many, Journal of Physics and Chemistry of Solids 26 (1965) 575.
[25] S. Johnsen, Z. Liu, J.A. Peters, J.H. Song, S.C. Peter, C.D. Malliakas, N.K. Cho, H.J. A.J. Freeman, B.W. Wessels, M.G. Kanatzidis, Chemistry of Materials 23 (2011) 3120.
[26] J. Clinton, Optimization and Characterization of a Novel Self Powered Solid State Neutron Detector, Rensselaer Polytechnic Institute (Doctoral thesis), 2011, pp. 73–78 (chapter 3).
[27] R. Dahal, K.C. Huang, J. Cliton, N. LiCausi, J.-Q. Lu, Y. Danon, I. Bhat, Applied Physics Letters 100 (2012) 243507.
[28] F.P. Doty, Advanced digital detectors for neutron imagining, Sandia Report SAND2003-8796 (Sandia National Laboratories, Livermore, 2003, Boron nitride solid-state neutron detector, US patent 6,727,504.

[29] J. Nikolic, A.M. Conway, C.E. Reinhardt, R.T. Graff, T.F. Wang, N. Deo, C.L. Cheung, Applied Physics Letters 93 (2008) 133502.

[30] S.L. Bellinger, W.J. McNeil, T.C. Unruh, D.S. McGregor, IEEE Transactions on Nuclear Science NS-56 (2009) 742.

[31] K.P. Ananthanarayanan, P.J. Gielisse, A. Choudry, Nuclear Instruments Methods 118 (1974) 45.

[32] P. Lunca-Popa, J.I. Brand, S. Balaz, L.G. Rosa, N.M. Boag, M. Bai, B.W. Robertson, P.A. Dowben, Journal of Physics D: Applied Physics 38 (2005) 1248.

[33] S. Adenwalla, P. Welsch, A. Harken, J.I. Brand, A. Sezer, B.W. Robertson, Applied Physics Letters 79 (2001) 4357.

[34] K. Osberg, N. Schemm, S. Balkir, J.O. Brand, M.S. Hallbeck, P.A. Dowben, M.W. Hoffman, IEEE Sensor Journal 6 (2006) 1531.